

Distance and Proper Motion Measurement of the Red Supergiant, S Persei, with VLBI H₂O Maser Astrometry

Y. Asaki^{1,2}

*Institute of Space and Astronautical Science, 3-1-1 Yoshinodai, Chuou, Sagamihara, Kanagawa 252-5210,
Japan*

asaki@vsop.isas.jaxa.jp

S. Deguchi³

Nobeyama Radio Observatory, Nobeyama, Minamimaki, Minamisaku 384-1305, Japan

deguchi@nro.nao.ac.jp

H. Imai⁴

*Department of Physics and Astronomy, Graduate School of Science and Engineering, Kagoshima
University, 1-21-35 Korimoto, Kagoshima 890-0065, Japan*

hiroimai@sci.kagoshima-u.ac.jp

K. Hachisuka⁵

Shanghai Astronomical Observatory, Chinese Academy of Sciences, Shanghai 200030, China

khachi@shao.ac.cn

M. Miyoshi⁶

*Division of Radio Astronomy, National Astronomical Observatory of Japan, 2-21-1 Osawa, Mitaka, Tokyo
181-8588, Japan*

makoto.miyoshi@nao.ac.jp

and

M. Honma⁷

*Mizusawa VLBI Observatory, National Astronomical Observatory of Japan, 2-21-1 Osawa, Mitaka, Tokyo
181-8588, Japan*

mareki.honma@nao.ac.jp

¹Institute of Space and Astronautical Science, 3-1-1 Yoshinodai, Chuou, Sagamihara, Kanagawa 252-5210, Japan

²Department of Space and Astronautical Science, School of Physical Sciences, The Graduate University for Advanced Studies (SOKENDAI), 3-1-1 Yoshinodai, Chuou, Sagamihara, Kanagawa 252-5210, Japan

³Nobeyama Radio Observatory, Nobeyama, Minamimaki, Minamisaku 384-1305, Japan

⁴Department of Physics and Astronomy, Graduate School of Science and Engineering, Kagoshima University, 1-21-35 Korimoto, Kagoshima 890-0065, Japan

⁵Shanghai Astronomical Observatory, Chinese Academy of Sciences, Shanghai 200030, China

⁶Division of Radio Astronomy, National Astronomical Observatory of Japan, 2-21-1 Osawa, Mitaka, Tokyo 181-8588, Japan

⁷Mizusawa VLBI Observatory, National Astronomical Observatory of Japan, 2-21-1 Osawa, Mitaka, Tokyo 181-8588, Japan

ABSTRACT

We have conducted VLBA phase-referencing monitoring of H₂O masers around the red supergiant, S Persei, for six years. We have fitted maser motions to a simple expanding-shell model with a common annual parallax and stellar proper motion, and obtained the annual parallax as 0.413 ± 0.017 mas, and the stellar proper motion as $(-0.49 \pm 0.23 \text{ mas yr}^{-1}, -1.19 \pm 0.20 \text{ mas yr}^{-1})$ in right ascension and declination, respectively. The obtained annual parallax corresponds to the trigonometric distance of $2.42^{+0.11}_{-0.09}$ kpc. Assuming the Galactocentric distance of the Sun of 8.5 kpc, the circular rotational velocity of the LSR at the distance of the Sun of 220 km s^{-1} , and a flat Galactic rotation curve, S Persei is suggested to have a non-circular motion deviating from the Galactic circular rotation for 15 km s^{-1} , which is mainly dominated by the anti rotation direction component of $12.9 \pm 2.9 \text{ km s}^{-1}$. This red supergiant is thought to belong to the OB association, Per OB1, so that this non-circular motion is representative of a motion of the OB association in the Milky Way. This non-circular motion is somewhat larger than that explained by the standard density-wave theory for a spiral galaxy, and is attributed to either a cluster shuffling of the OB association, or to non-linear interactions between non-stationary spiral arms and multi-phase interstellar media. The latter comes from a new view of a spiral arm formation in the Milky Way suggested by recent large N-body/smoothed particle hydrodynamics numerical simulations.

Subject headings: stars: supergiants, masers, Galaxy: structure

1. Introduction

Phase-referencing VLBI technique is capable of determining positions of celestial objects relative to background calibrators with sub-milliarcsecond accuracy (Bartel et al. 1986). Absolute position changes of Galactic maser sources can be directly detected on the sky using this technique, and the observables are very useful for measuring annual parallaxes or trigonometric distances to the sources and their proper motions (e.g., Xu et al. 2006; Hachisuka et al. 2006). In addition, the measured trigonometric distance and proper motion together with the radial velocity of a source can provide us a complete three-dimensional kinematic information without model assumptions.

There are a number of Galactic evolved stars with circumstellar H₂O masers, which are observable with VLBI at 22 GHz. The red supergiant, S Persei (hereafter, S Per), is one such target harboring H₂O masers as well as SiO and OH masers (e.g., Alcolea et al. 1990; Richards 1996). This star is separated by 1.5° from a double cluster, h and χ Persei (hereafter, $h + \chi$ Per, see Figure 1), located at the outer edge of the Perseus arm, which involves a large group of more than 20 red supergiant stars. The cluster is the most massive open cluster within 3 kpc from the Sun and belongs to the OB association, Per OB1. Humphreys (1975) reported that the radial velocity of S Per is fairly

consistent with that of $h + \chi$ Per, so that S Per is thought to belong to the OB association. We can therefore determine the distance and three-dimensional motion of the OB association in the spiral arm by measuring the annual parallax and proper motion of the member star.

We report results of phase-referencing VLBI monitoring of the H₂O masers associated with S Per over six years with the Very Long Baseline Array (VLBA) of the National Radio Astronomy Observatory (NRAO). The observations are described in Section 2. Data reduction including astrometric analyses is presented in Section 3. The results are presented in Section 4. We discuss the results in Section 5 and summarize this study in Section 6. The results presented here replace those reported previously by Asaki et al. (2007a). In this paper, we define that the Local Standard of Rest (LSR) is a reference frame at the position of the Sun and moving in a circle around the center of the Milky Way. We adopt the IAU standard values for the Galactocentric distance of the Sun, $R_0 = 8.5$ kpc, and the circular rotational velocity of the LSR at the distance of the Sun, $\Theta_0 = 220 \text{ km s}^{-1}$. We also assume a flat Galactic rotation curve around the Sun. For almost all the parts, we adopt a Solar motion of 20 km s^{-1} relative to the LSR to the direction of $(\alpha_{1900}, \delta_{1900}) = (18^{\text{h}}, 30^\circ)$ for the radial velocity (radio definition

of the LSR). Hereafter this Solar motion is referred to as the standard Solar motion, and the LSR with the standard Solar motion is referred to as the traditional LSR. In the following analyses, we adopt the systemic velocity of S Per of -38.5 km s^{-1} (Diamond et al. 1987) in the traditional LSR. On the other hand, because the Galactic parameters are known to involve some uncertainties (McMillan & Binney 2010), we discuss the observational results adopting more realistic values for the Solar motion in Section 5.2, which was determined from the average motion of a number of stars in the solar neighborhood observed with the Hipparcos satellite. For the proper motion, we adopt the heliocentric coordinates.

2. Observations

Figure 1 shows sky positions of the observed sources. VLBI phase-referencing observations of S Per at 22.2 GHz have been conducted together with a closely located continuum source as a positional reference at a separation angle of 0.2° . This positional reference source was initially selected from the 6-cm northern sky catalogue (Becker et al. 1991) and the Texas survey (Douglas et al. 1996). Later we found that this source is catalogued under the number 143 in the 21-cm radio continuum survey of the Galactic plane by Kallas & Reich (1980) (the so-called “KR survey”) and an outer Galaxy VLA survey by Fich (1986) based on the KR survey, so that the source is referred to hereafter as KR143. Imai (2001) for the first time confirmed that KR143 is detectable with VLBI observations at 22 GHz, while we could not find an optical counterpart for KR143. We have conducted a total of eight-epoch VLBI observations over six years with the ten VLBA antennas. The observing epochs are listed in Table 1.

Two intermediate-frequency (IF) bands with 16-MHz bandwidth in left-hand circular polarization were recorded. These IF bands are continuous in frequency. The H_2O maser emissions of S Per has been received with the lower IF band (IF1) while the upper IF band (IF2) was used to improve the Signal-to-Noise Ratio (SNR) for KR143. We have also conducted phase-referencing observations of a pair of KR143 and ICRF 0244+624 with a separation angle of 4.8° in the last five epochs to check the position stability of KR143 with re-

spect to the positionally reliable ICRF source. A larger separation angle will take a longer telescope slew time, and therefore a longer switching duty cycle. In general, the larger the separation angle and/or the longer the switching duty cycle is, the more difficult is phase-referencing at 22 GHz due to stochastic tropospheric phase fluctuations. We selected a lower observing frequency of 15.3 GHz for the pair of KR143 and ICRF 0244+624 to reduce a coherence loss effect due to the tropospheric phase fluctuations. The switching cycle time, t_s , for the phase-referencing is listed in Table 1.

In the first three epochs, 20-min phase-referencing sequence at 22 GHz was interleaved by 2- to 3-min calibrator observations. In the last five epochs, 20-min phase-referencing sequences at 22 GHz and 15 GHz were conducted in turn, and each sequence was interleaved by short calibrator scans at the same frequency. VLBI cross-correlation was carried out at the VLBA correlation center in Socorro to generate VLBI fringe data with 1024-frequency channels, corresponding to a velocity resolution of 0.2107 km s^{-1} . In the first-epoch cross correlation, a wrong position with an offset by 4 arcsec was used as a phase tracking center of S Per. This mistake was recovered in the course of data reduction process. The observed pairs of sources in our monitoring program are listed in Table 2 together with their separation angles.

3. Data reduction

We analyzed the VLBI data using the standard NRAO data reduction software, Astronomical Image Processing Software (AIPS), version 31DEC06. There were two data reduction series: one for the pair S Per and KR143, and another one for the pair KR143 and ICRF 0244+624.

3.1. Initial calibrations

Initial calibration tasks were common for both the pairs of sources. First, the amplitude calibration was conducted by using the measured system noise temperatures and gain variation data. In the next step, Earth Orientation Parameters (EOP) errors, two-bit sampling bias in the analogue-to-digital (A/D) conversion in VLBI signal processing, antenna parallactic angles, and ionospheric dispersive delays were corrected.

In the first three epochs, NRAO 150, J0102+5824

and 3C 84 have been observed as calibrators at 22.2 GHz, while the former two have been observed as calibrators in the last five epochs. At 15.3 GHz, NRAO 150 and J0102+5824 have been observed as calibrators in the last five epochs. Among them, NRAO 150 was used both in the data reduction series for calibrating relative clock offsets and phase offsets between the independent antennas. Phase differences between the two IF bands were also removed by using the NRAO 150 fringe data. In the next steps of data analysis, a customized data reduction path was used for each pair of the sources.

3.2. Data reduction for S Per and KR143 at 22 GHz

For the maser data analysis, the Doppler shift in S Per spectra due to the Earth rotation and Earth’s Kepler motion were corrected with the AIPS spectrum channel correction task, CVEL. The observed frequencies of the maser lines were converted to radial velocities with respect to the traditional LSR using the rest frequency of 22.235080 GHz for the H₂O 6₁₆ – 5₂₃ transition. The spectrum deformation due to the receiver complex gain characteristics was calibrated with the NRAO 150 spectrum in the CVEL process.

The 4 arcsec error in the position of S Per’s phase tracking center in the first epoch was corrected with the AIPS visibility phase correction task UVFIX. Note that, although the S Per visibilities might be subject to the coherence loss as a result of the cross correlation task with the phase tracking center error, the following astrometric analysis is not affected.

We inspected the cross-power spectra for all the baselines in order to select frequency channels of emission which would be unresolved and not have rapid amplitude–time variation. We then carried out fringe-fitting by using the AIPS task FRING, with an option of no delay search for the selected channel. The fringe-fitted data were image-synthesized with a 50- μ as pixel for a region of 4096×4096 pixels, roughly a 200×200 -square mas region by using the AIPS task IMAGR. Using this image as an initial model, phase and amplitude self-calibration was conducted.

With the above processes from the fringe-fitting to the self-calibration, we obtained the complex

gain calibration data, which were applied to the remaining frequency channels to make image cubes for the same maser region. The images were produced for all channels separately in the velocity range of -23 and -61 km s⁻¹ with the step of 0.2107 km s⁻¹ in the traditional LSR. To pick up maser emission initially, we used the 2-D Gaussian component survey task SAD in each velocity channel map. Based on the results of SAD, we visually inspected the surveyed Gaussian components one by one. We stored the image pixels larger than $3\text{-}\sigma$ noise level for a visually confirmed maser emission. Hereafter we define a maser “spot” as an emission in a single velocity channel, and a maser “feature” as a group of spots observed in at least two continuous velocity channels at a coincident or very closely located positions.

For KR143 imaging, the Doppler correction and bandpass calibration were skipped because the spectrum was averaged for the continuum source. Since there was no S Per’s maser emission in IF2, the complex gain calibration data for IF1 was applied to IF2, whose phase and delay biases from IF1 was already removed in the initial calibration. The synthesized image of KR143 with the pixel size of 50 μ as was obtained by using two IF bands, so that the image SNR is higher than that with the single IF band by a factor of $\sqrt{2}$. The SNR of KR143 phase-referenced images ranges between 18 and 37 at 22 GHz.

3.3. Data reduction for KR143 and ICRF 0244+624 at 15 GHz

The Doppler and bandpass correction were skipped for both sources in processing of the 15 GHz data as unnecessary. ICRF 0244+624 was imaged with the 50- μ as pixel size to obtain the complex gain calibration data. This calibration data were applied to the KR143 fringe at 15 GHz before imaging. Synthesized images of KR143 were made with the 50- μ as pixel size. The SNR of KR143 phase-referenced images ranges between 7 and 17 at 15 GHz.

4. Results

4.1. KR143’s position

Phase-referenced radio maps of KR143 are dominated by a weak single component both at 15 and 22 GHz. For the present astrometric study,

we firstly determined the position of KR143 with respect to ICRF 0244+628 at 15 GHz, which had not been determined to high precision previously. In this paper, the position of ICRF 0244+624 in J2000 is adopted as $2^{\text{h}}44^{\text{m}}57^{\text{s}}.696746$ and $+62^{\circ}28'6''.515030$ in right ascension and declination, respectively. Since ICRF 0244+624 has shown a very simple structure in the radio maps, we treated the peak position of the image as a positionally stable point in the sky. We assume that KR143's position at 22 GHz is consistent with that at 15 GHz, and astrometric analysis of S Per was determined with respect to this position.

Since images of KR143 have rather low SNR, a Gaussian fitting for the detected component may be affected by a rather severe image distortion due to a high image noise even if the object consists of only a single component. In addition, the phase-referencing image may be distorted by the residual phase errors, introduced, e.g., by the static tropospheric delays. We used the peak position of KR143's image as the positional reference in order to minimize those effects in determining the position. The position measurement error was calculated from the beamwidth over the SNR at the peak.

For the astrometric measurements of Galactic sources, a positional reference should be a background extragalactic source such as an Active Galactic Nuclei (AGN). However, because we hardly know whether KR143 is a suitable background source, we then investigated how positionally stable KR143 is with respect to ICRF 0244+624. Figure 2 shows a time variation of the KR143's position in the last five epochs of our experiment. Assuming that KR143 is a Galactic source for which the annual parallax is significant, we carried out a Levenberg-Marquardt non-linear least-square analysis to obtain the annual parallax and proper motion, but could not find a reliable solution because the χ^2 value per degree of freedom was quite large, no less than 57. This suggests that the annual parallax and proper motion are below our threshold because KR143 is sufficiently far from the Sun. This threshold is determined by the accuracy of the relative position measurements in phase-referencing for the pair of the sources. Figure 2 also displays a sinusoidal pattern of our least-square analysis result as well as another sinusoidal pattern for a source at the

distance of 4 kpc, for comparison.

The spatial distribution of the image peaks of KR143 at 15 GHz are shown in the top plot of Figure 3. This plot also shows the $1\text{-}\sigma$ ellipse (a solid line). One possible reason for the observed change position of the peaks is inaccuracies in the VLBI correlator model for the phase-referencing astrometry for the pair of the observed sources. We conducted Monte Carlo phase-referencing observation simulations for the pair of KR143 and ICRF 0244+624 to examine whether the observed position change could be explained by the uncertainties of the VLBI correlator model. For generating simulated phase-referencing fringes, we used a VLBI observation simulator, ARIS (Astronomical Radio Interferometer Simulator, Asaki et al. 2007b). In the simulations, we assume flux densities of KR143 and ICRF 0244+624 of 20 and 500 mJy, respectively, which were determined from our observations. The sources were assumed to be point-like sources. The simulated observation schedule and observing system settings such as the recording bandwidth and A/D quantization level were adopted from actual VLBA observations. There were two simulation series: one included $1\text{-}\sigma$ static tropospheric excess path length error to the zenith (zenith EPL error) of 3 cm (e.g., Reid et al. 1999), and the other one used the zenith EPL error of 6 cm. We made 100 trials for each of the zenith EPL error cases. The simulation results are shown in the middle and bottom plots of Figure 3 for the $1\text{-}\sigma$ zenith EPL error of 3 and 6 cm, respectively. In the case of a zenith EPL error of 6 cm, the simulation results are consistent with the observation results. Since some of our observations were conducted during the summer period, it is quite natural that the zenith EPL error would be around 6 cm. We conclude that the KR143's position change is mainly due to the zenith EPL error of several centimeters in the VLBI correlator model. Hereafter we refer a relative position error for a pair of point sources with the phase-referencing due to uncertainties in a VLBI correlator model for the atmospheric EPL, antenna positions, EOP, and other phase error factors as an astrometric error.

The measured flux densities of KR143 are shown in Figure 4 together with the data from the previous work by Douglas et al. (1996), Kallas & Reich (1980), Condon et al. (1998), Becker et

al. (1991), Fich (1986), and Imai (2001). Note that, for the measurements of the flux density of KR143 from our radio images, we conducted a phase-self-calibration process. Figure 4 resembles a synchrotron power-law spectrum, making it very likely that KR143 is an AGN. Although there is currently no concrete evidence that KR143 is not located in or near our Galaxy because of the unknown redshift, we assume throughout this paper that KR143 is an AGN. The relative position of KR143 on the sky with respect to ICRF 0244+624 is determined with the standard errors of 61 and 116 μas in right ascension and declination, respectively, from all the five epochs. The absolute position of KR143 is listed in Table 3.

4.2. Astrometry of S Per

In the phase-referencing astrometric analysis for S Per, we investigated the time variation of the peak positions of the maser spots with respect to the peak position of the 22-GHz phase-referenced radio image of KR143. To estimate the astrometric error with the VLBI phase-referencing for the pair of S Per and KR143, we conducted Monte Carlo simulations of phase-referencing observations for the pair of these sources at 22.2 GHz with ARIS. In the simulations, we assumed that flux densities of S Per and KR143 of 1 Jy and 20 mJy, respectively, and that S Per was a continuum source. The tropospheric zenith EPL error of 6 cm was set as found in the simulation described above for the pair of KR143 and ICRF 0244+624. Due to the small separation angle and fast antenna switching, the simulations show that the $1\text{-}\sigma$ errors in the relative position are 6 μas and 14 μas in right ascension and declination, respectively. We used these standard deviations to provide the astrometric error for the pair of the sources in the following analysis.

Figure 5 shows the spatial distribution of the H_2O maser emission of S Per for all the epochs. The maser emission is spread within a roughly circular structure with a radius of about 60 mas. We identified 77 maser features consisting of 478 maser spots in all the available epochs. For obtaining the trigonometric parallax and proper motion of the star, we conducted the following four steps. Firstly, we selected a limited number of maser spots to evaluate the annual parallax. Our selection criteria are as follows: (1) maser spots

at epochs D, E, F, and G were all detected at the same velocity channel with the SNR of at least 6; (2) in addition to the above epochs, they were detected with the SNR of at least 6 at least at one of the other epochs at the same velocity channel; (3) no significant velocity drift larger than $0.25 \text{ km s}^{-1} \text{ yr}^{-1}$ was observed for the features involving the selected spots; and (4) morphology does not significantly change between the epochs. We selected 44 maser spots from eight maser features.

Secondly we carried out the Levenberg-Marquardt least-square analysis for the i -th maser spot to obtain the initial position, $(\Delta\alpha_A^i, \Delta\delta_A^i)$, at epoch A, the constant proper motion, $(\mu_\alpha^i \cos \delta, \mu_\delta^i)$, along with the annual parallax, π^i , both in right ascension and declination. In the initial trial, reduced χ^2 values of the analysis were in the range from a few tens to a few hundreds. These large values indicate that there must be unaccounted errors in the analysis. As explained above, we expect that the astrometric error in our observation is 6 and 14 μas for right ascension and declination, respectively. On the other hand, internal morphological time variations of the maser features during the monitoring period of over six years cannot be negligible, as already pointed out in previous studies (e.g., Imai et al. 2007). For diagnostic purposes, we added position uncertainties of 0.2 mas for epochs A and H, 0.1 mas for epochs B and C, and 0.05 mas for epochs D, E, F, and G to the astrometric error both for right ascension and declination. This resulted in making the reduced χ^2 values equal to unity in our least-square analysis. This additional position uncertainty which we attribute to the unpredicted time variations in maser morphology is referred to hereafter as a maser morphology uncertainty. Table 4 lists the least-square analysis results for each of the selected maser spots. Figure 6 shows the analysis result of one of the maser spots (spot-ID 39 in Table 4). Figure 7 shows the histogram of the evaluated annual parallaxes for the 44 maser spots. The weighted average of the evaluated annual parallaxes is $0.414 \pm 0.006 \text{ mas}$.

We thirdly conducted a combined fitting with our least-square analysis for the 44 maser spots to obtain the trigonometric distance to S Per. In this step, we assumed that all the maser spots have a common annual parallax, π^* , which is one of

the fitting parameters. This combined fitting result for π^* is 0.413 mas, almost identical to the weighted average of the 44 annual parallaxes. The parameter fitting error in π^* was 0.006 mas from a covariance matrix of our least-square analysis.

In obtaining the annual parallax, two systematic errors have to be considered. One is the astrometric error, and the other one is the maser morphology uncertainty which provides a common position offset to the member spots in a certain maser feature. The most conservative estimate of the obtained annual parallax error becomes 0.040 mas, which is calculated from the above statistical error of 0.006 mas multiplying by a factor of $\sqrt{44}$ under an assumption that the position error of the selected maser spots are not independent. Hachisuka et al. (2009) applied a method to average positions of a number of maser spots from three features of W3(OH) water masers before their parallax fitting in order to avoid the maser morphology uncertainty, and achieved a 6- μ as accuracy in the annual parallax measurement. We note that the impact of the astrometric error on the annual parallax measurement is not reduced even if a number of maser features are simultaneously processed. On the other hand, the impact of the maser morphology uncertainty can be reduced in processing multiple maser features because the position offset due to this error becomes randomized. Since there are eight maser features in our analysis, the error quantity of 0.040 mas is over estimated. Figure 8 shows the position residuals of the selected 44 maser spots after removing the obtained annual parallax of 0.413 mas, proper motions and initial positions. It is noticed that, although a small positive trend can be seen in right ascension at epoch D, there are not apparently obvious systematic errors at central four epochs from D to G. It is also recognizable that systematic errors are partially seen for specific maser features possibly due to the time variations in the maser morphology (see, for example, spot-ID 41-44 (feature-ID 8) at epochs D, E, and F).

To evaluate contributions of those systematic errors to the obtained annual parallax, we conducted simulations of the combined fitting analysis by using fake data sets imitating the selected maser spots with the position measurement error, astrometric error, and maser morphology uncertainty. A random position offset due to the po-

sition measurement error to each maser spot at each epoch. A position offset due to the astrometric error is applied to all the maser spots at each epoch. A position offset due to the maser morphology uncertainty is applied to all the maser spots included in each of the eight maser features at each epoch. We investigated the following error cases: (1) only position measurement error; (2) only astrometric error; (3) only maser morphology uncertainty; and (4) a combination of all the three errors above. We generated 100 data sets for each of the four cases and carried out the Levenberg-Marquardt least-square analysis. Root-mean-square errors from the average of the 100 obtained annual parallaxes were 3, 9, 15, and 17 μ as for the cases of 1, 2, 3, and 4, respectively. The maser morphology uncertainty dominates the annual parallax error in our combined fitting while the astrometric error corresponds to a relatively small part. It is reasonable to adopt the value of 17 μ as as an upper limit of the trigonometric distance uncertainty, corresponding to the trigonometric distance of $2.42^{+0.11}_{-0.09}$ kpc. We then conducted our least-square analysis to obtain individual proper motions of all the 478 maser spots with π^* .

The obtained proper motions of the maser spots are considered to be a combination of an expanding flow of the circumstellar envelop (CSE) and the proper motion of the red supergiant in the Milky Way. We finally conducted a model fitting analysis assuming a spherically expanding flow model described by Imai et al. (2000) and Imai et al. (2003). In the model fitting, we estimated the distribution centroid indicating the stellar position as well as the stellar proper motion separated from the expanding shell motion of the CSE. We obtained the stellar proper motion in right ascension as $\mu_\alpha^* \cos \delta = -0.49 \pm 0.23$ mas yr $^{-1}$, and in declination as $\mu_\delta^* = -1.19 \pm 0.20$ mas yr $^{-1}$. This proper motion is consistent with that listed in the Tycho-2 Hipparcos catalogue, $(-0.1 \pm 1.8, -2.8 \pm 1.8)$ mas yr $^{-1}$, within its uncertainty (Hog et al. 2000). The centroid of the maser distribution was determined with an accuracy of 8 mas in both right ascension and declination. Results of our astrometric analysis for S Per are listed in Table 5. A residual time variation of the maser emission after removing the annual parallax and stellar proper motion is shown in Figure 9. Internal proper mo-

tions of the identified 478 maser spots are shown in Figure 10 along with their radial velocities.

5. Discussions

5.1. Distance to S Per

Our monitoring program determined the trigonometric distance to S Per to be $2.42_{-0.09}^{+0.11}$ kpc without model assumptions. Marvel (1996) estimated a distance to this star as 2.3 ± 0.5 kpc by means of a *statistical parallax* method, in which relative proper motions of the H₂O maser spots are fitted to an expanding shell where proper motions of the outermost spots are equal to the radial velocities of the maser spots with no significant proper motions. The statistical parallax distance coincides with the trigonometric one within the measurement uncertainties. The trigonometric parallax greatly improved the accuracy of the distance: the uncertainty is five times better than that of the statistical parallax.

S Per is considered to belong to Per OB1 because the radial velocity of S Per is consistent with that of this OB association (Bidelman 1947). The double cluster, $h + \chi$ Per, whose distance was determined to be 2.34 kpc with the 2-percent accuracy from the H-R diagram (Slesnick et al. 2002) is also included in Per OB1, so that S Per is in the vicinity of the double cluster in the OB association. The apparent radius of Per OB1 is about 4° , corresponding to a ~ 170 -pc radius at the distance of $h + \chi$ Per. S Per is located on the far side of Per OB1.

Recent VLBI astrometric observations of Galactic H₂O and CH₃OH maser sources in the Perseus arm have been used to measure their trigonometric distances. Figure 11 shows the locations of such Galactic masers close to S Per in the Perseus arm in a face-on view of the Milky Way (Xu et al. 2006; Sato et al. 2008; Moellenbrock et al. 2009; Moscadelli et al. 2009; Reid et al. 2009a). In the figure, we depict only the H₂O masers for NGC 281 West; measurements using the methanol masers result in a smaller trigonometric distance than using the H₂O masers (Rygl et al. 2010). From this figure, it is clear that S Per, as well as NGC 281 West, are located at the outer edge of the Perseus arm. Assuming a pitch angle of the spiral arm of 16.5° (Reid et al. 2009b), we can estimate the width of the Perseus arm from

the difference in locations between the outer edge maser sources and those located in the inner part of the arm. Hence, the estimated width of the Perseus arm is at least ~ 0.7 kpc.

5.2. Three-dimensional motion of S Per in the Milky Way

The stellar proper motion of S Per enables us to discuss the three-dimensional kinematics of the evolved star in the Milky Way. In this subsection, we use realistic values of the Solar motion¹, $(U_\odot, V_\odot, W_\odot) = (7.5, 13.5, 6.8)$ km s⁻¹ (Francis & Anderson 2009; see also discussions in McMillan & Binney 2010). Let us estimate a non-circular motion of S Per in LSR at the red supergiant. This star has a rather large non-circular motion of 15 km s⁻¹ at the Galactocentric distance of 10.4 kpc: the non-circular velocity components are 3.3 ± 2.3 km s⁻¹ toward the Galactic center, 12.9 ± 2.9 km s⁻¹ toward the anti-direction of the Galactic rotation, and 6.3 ± 3.1 km s⁻¹ toward the south pole.

Recent VLBI astrometric observations of Galactic maser sources have revealed large non-circular motions of several objects in the Perseus arm. Figure 11 presents the non-circular velocity components of S Per along with those from other maser objects in the Perseus arm. Although this non-circular motion is not sensitive to R_0 and Θ_0 with the 10-percent variation, we have to admit that, if there is a 10-percent dip in the Galactic rotation curve at the Galactocentric distance of 9–10 kpc (Sofue et al. 2009), the lag of S Per from the Galactic rotation (V component) becomes smaller. However, such a rotation curve cannot remove all the observed non-circular motions of the maser sources in the Perseus arm, or even makes several of them larger. Moreover, such peculiar motions can be found for Galactic masers in star forming regions (SFRs) not only along the Perseus arm, but also along the local spur, Outer and Inner arms (Reid et al. 2009b; Rygl et al. 2010). These two papers also discuss a large lag of the V component of the SFRs from a flat rotation curve together with a Hipparcos Solar motion

¹ U_\odot is the velocity component directed to the Galactic center, V_\odot is the component toward the circular rotational direction in the Galactic plane, and W_\odot is the component perpendicular to the Galactic plane and directed to the Galactic north pole.

of Dehnen & Binney (1998). On the other hand, McMillan & Binney (2010) reanalyzed the samples published by Reid et al. (2009b) in order to estimate the Galactic rotation as well as the Solar motion. Their fitting result of the V_{\odot} component of 11 km s^{-1} , instead of 5.2 km s^{-1} of Dehnen & Binney (1998), can reduce such the large lags. However the Galactic SFRs still seems to have $10 - 20 \text{ km s}^{-1}$ peculiar motions even with the revised Solar motion, and those non-circular velocity components in the Galactic plane somehow show randomness. These non-circular motions do not quantitatively match a standard understanding of the stationary density-wave theory (Lin & Shu 1964) and a standing galactic shock solution in a tight-winding spiral potential (Roberts 1969; Roberts & Yuan 1970).

One of the reasons for such peculiar motions may be attributed to an intrinsic space motion of each SFR. Lee & Lim (2008) found that there are new SFRs in the southern H_{I} shell in Per OB1, and that the new stars have larger southern velocities due to the up-to-date cloud shuffling caused by $h + \chi$ Per. According to the cloud-shuffling model, a molecular cloud is swept up by UV radiation pressure from nearby OB stars, perhaps together with supernova explosions. Star formations are triggered in the cloud to form OB associations. At the same time, the compressed cloud will be accelerated in the anti-direction to the original sources causing the cloud shuffling. Cappa & Herbstmeier (2000) reported on an H_{I} superbubble with 2° -radius centered at $h + \chi$ Per. However, S Per, located inside the superbubble, does not move away from the double cluster, so that this star does not seem to be formed in a process of the cloud shuffling caused by $h + \chi$ Per.

Although we cannot find a trace of cluster shuffling sources other than $h + \chi$ Per at this moment, the cloud shuffling model still provides us an attractive idea in order to explain the large non-circular motion of the OB association and S Per. It is interesting that Lee & Lim (2008) also reported that proper motions of stars in Per OB1 based on the Hipparcos measurements show a velocity component downward to the Galactic plane (toward the South Galactic pole), so that the non-circular motion of S Per may be representative of a motion of the molecular cloud in which the OB stars and S Per were formed. The plausible sce-

nario is as follows: Considering the age of $h + \chi$ Per is $12.8 \pm 1.0 \text{ Myrs}$ (Slesnick et al. 2002), a cloud shuffling took place near the precursor molecular cloud of Per OB1 around a few tens of Myrs ago because of radiation pressure from precedent OB stars and/or supernova explosions in the Galactic plane. The molecular cloud later forming Per OB1 has been accelerated in the out-of-disk direction. S Per was formed in the molecular cloud ahead of a large SFR around the double cluster. This cloud shuffling also might affect the in-disk non-circular motions of the cloud. Another item of observational evidence for a cloud shuffling causing the non-circular motion was provided by Sato et al. (2008) and Rygl et al. (2010) for NGC 281 West. It was suggested that large non-circular motions of NGC 281 West masers were due to the supershell generated by supernova explosions.

Another new idea to explain the non-circular motions of the Galactic SFRs arises from large N-body/hydrodynamics numerical simulations. Baba et al. (2009) showed that, with their high-resolution numerical model of a spiral galaxy and their original N-body/gas simulation code (Saitoh et al. 2009), the non-circular motions of the SFRs were explained by natural consequence of non-linear interactions between non-stationary spiral arms and multi-phase interstellar media. With their numerical simulations of a disk galaxy, they found that young stars with ages $\leq 50 \text{ Myr}$ in a spiral galaxy have large and random non-circular motions. This idea can be applied to S Per and Per OB1 because the ages of those objects are younger than 50 Myr . The N-body+hydrodynamics simulations also revealed that molecular clouds in a spiral galaxy can have a velocity dispersion of several km s^{-1} in the vertical direction to the disk (J. Baba, 2009, private communications), so that a rather large peculiar motion of Per OB1 vertical to the Galactic plane could be explained without a cloud shuffling. Since we have quite limited samples with the measurable non-circular motions of the young objects in the Milky Way, it is very important to measure the distances and proper motions of the spiral arm objects to compare with those simulation results. A deep understanding of the dynamics of the Galactic spiral arms and the origin of the non-circular motions of SFRs will be possible in near future when massive numerical simulations can

be combined with a much larger amount of VLBI astrometry samples.

6. Conclusions

We have conducted phase-referencing VLBI monitoring for the Galactic red supergiant, S Per. The distance to S Per was determined to be $2.42_{-0.09}^{+0.11}$ kpc based on the trigonometric parallax. Together with the stellar radial velocity and obtained proper motion, we investigated the three-dimensional motion of S Per in the Milky Way, showing the non-circular motion of 15 km s^{-1} from the Galactic circular rotation, which is mainly dominated by the anti rotation direction component of $12.9 \pm 2.9 \text{ km s}^{-1}$. This non-circular motion may be representative of the motion of the young star cluster, Per OB1, in the Milky Way. Recent large N-body/hydrodynamics numerical simulations show that the non-circular motions of star forming regions are not exceptional but can be seen everywhere in a spiral galaxy. The cloud shuffling is another plausible mechanism to give such a large non-circular motion to the Per OB1 association. To reveal these non-circular motions as well as the other maser sources on the spiral arms, a lot of sample points are needed. In the near future, we will be able to obtain a set of trigonometric measurements with the three-dimensional motions of the maser sources with phase-referencing VLBI. We will be able to investigate the galactic structure along with its kinematics with a support of the large-scale N-body/hydrodynamics numerical simulations.

The authors acknowledge the referee for carefully reading our paper and giving us many fruitful comments. The authors also express their deep gratitude to the VLBA of the NRAO. The VLBA/NRAO is a facility of the National Science Foundation, operated under a cooperative agreement by Associated Universities, Inc. Y. Asaki would like to thank J. Baba, K. Wada, J. Makino, and T. Saito of NAOJ for suggestions about the Galactic rotation. H. Imai was financially supported by Grant-in-Aid for Scientific Research from Japan Society for Promotion Science (20540234).

REFERENCES

- Alcolea, J., Bujarrabal, V., & Gómez-González, J. 1990, *A&A*, 231, 431
- Asaki, Y., Deguchi, S., Imai, H., Hachisuka, K., Miyoshi, M., & Honma, M. 2007a, in *IAU Symposium*, Vol. 242, ed. J. M. Chapman & W. A. Baan, 378
- Asaki, Y., et al. 2007b, *PASJ*, 59, 397
- Baba, J., Asaki, Y., Makino, J., Miyoshi, M., Saitoh, T. R., & Wada, K. 2009, *ApJ*, 706, 471
- Bartel, N., Herring, T. A., Ratner, M. I., Shapiro, I. I., & Corey, E. 1986, *Nature*, 319, 733
- Bidelman, W. P. 1947, *ApJ*, 105, 492
- Becker, R. H., White, R. L., & Edwards, A. L. 1991, *ApJS*, 75, 1
- Cappa, C. E., Herbstmeier, U. 2000, *AJ*, 120, 1963
- Condon, J. J., Cotton, W. D., Greisen, E. W., Yin, Q. F., Perley, R. A., Taylor, G. B., & Broderick, J. J. 1998, *AJ*, 115, 1693
- Diamond, P. J., Johnston, K. J., Chapman, J. M., Lane, A. P., Bowers, P. F., Spencer, J. H., & Booth, R. H., 1987, *A&A*, 174, 95
- Douglas, J. N., Bash, F. N., Bozayan, F. A., Torrence, G. W., & Wolfe, C. 1996, *AJ*, 111, 1945
- Dehnen, W., & Binney, J. J. 1998, *MNRAS*, 298, 387
- Fich, M. 1986, *AJ*, 92, 787
- Francis, C., & Anderson, E. *New Astronomy*, 14, 615, 2009
- Georgelin, Y. M., & Georgelin, Y. P. 1976, *A&A*, 49, 57
- Hachisuka, K., et al. 2006, *ApJ*, 645, 337
- Hachisuka, K., Brunthaler, A., Menten, K. M., Reid, M. J., Hagiwara, Y., & Mochizuki, N. 2009, *ApJ*, 696, 1981
- Hog et al. 2000, *A&A*, 355, 27
- Humphreys, R. 1975, *PASP*, 87, 433

- Imai, H., Kameya, O., Sasao, T., Miyoshi, M., Deguchi, S., Horiuchi, S., & Asaki, Y. 2000, *ApJ*, 538, 751
- Imai, H., 2001, *Journal of the Comm. Res. Lab.*, 48, 31
- Imai, H., et al. 2003, *ApJ*, 590, 460
- Imai, H., et al. 2007, *PASJ*, 59, 1107
- Kallas, E. & Reich, W. 1980, *A&AS*, 42, 227
- Lee, H-T., & Lim, J. 2008, *ApJ*, 679, 1352
- Lin, C. C., & Shu, F. H. 1964, *ApJ*, 140, 646
- Marvel, K. B. 1996, PhD thesis, New Mexico State Univ., New Mexico, ch.3
- McMillan, P. J., & Binney, J. J. 2010, *MNRAS*, 402, 934
- Moellenbrock, G. A., Claussen, M. J., & Goss, W. M. 2009, *ApJ*, 694, 192
- Moscadelli, L., Reid, M. J., Menten, K. M., Brunthaler, A., Zheng, X. W., & Xu, Y. 2009, *ApJ*, 693, 406
- Nakanishi, H., & Sofue, Y. 2006, *PASJ*, 58, 847
- Reid, M. J., Readhead, A. C. S., Vermeulen, R. C., & Treuhaft, R. N. 1999, *ApJ*, 524, 816
- Reid, M. J., Menten, K. M., Brunthaler, A., Zheng, X. W., Moscadelli, L., & Xu, Y. 2009a, *ApJ*, 693, 397
- Reid, M. J., et al. 2009b, *ApJ*, 700, 137
- Richards, A. M. S., Yates, J. A., & Cohen, R. J. 1996, *MNRAS*, 282, 665
- Roberts, W. W. 1969, *ApJ*, 158, 123
- Roberts, Jr., W. W., & Yuan, C. 1970, *ApJ*, 161, 887
- Rygl, K. L. J., Brunthaler, A., Menten, K. M., van Langevelde, H. J., & Xu, Y. 2010, *A&A*, 511, A2
- Saitoh, T. R., et al. 2009, *PASJ*, 61, 481
- Sato, M., et al. 2008, *PASJ*, 60, 975
- Slesnick, C. L., Hillenbrand, L. A., & Massey, P. 2002, *ApJ*, 576, 880
- Sofue, Y., Honma, M., & Omodaka, T. 2009, *PASJ*, 61, 227
- Xu, Y., Reid, M. J., Zheng, X. W., & Menten, K. M. 2006, *Science*, 311, 54

This 2-column preprint was prepared with the AAS L^AT_EX macros v5.2.

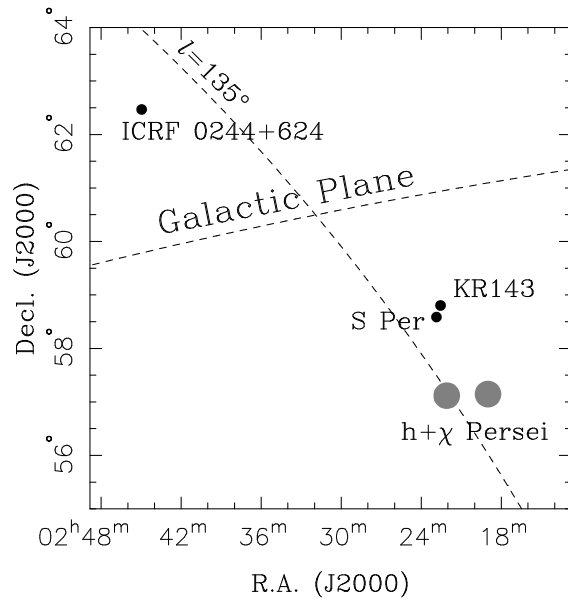


Fig. 1.— Sky position of the observed sources in the present VLBI phase-referencing monitoring. The position of $h + \chi$ Per is also indicated.

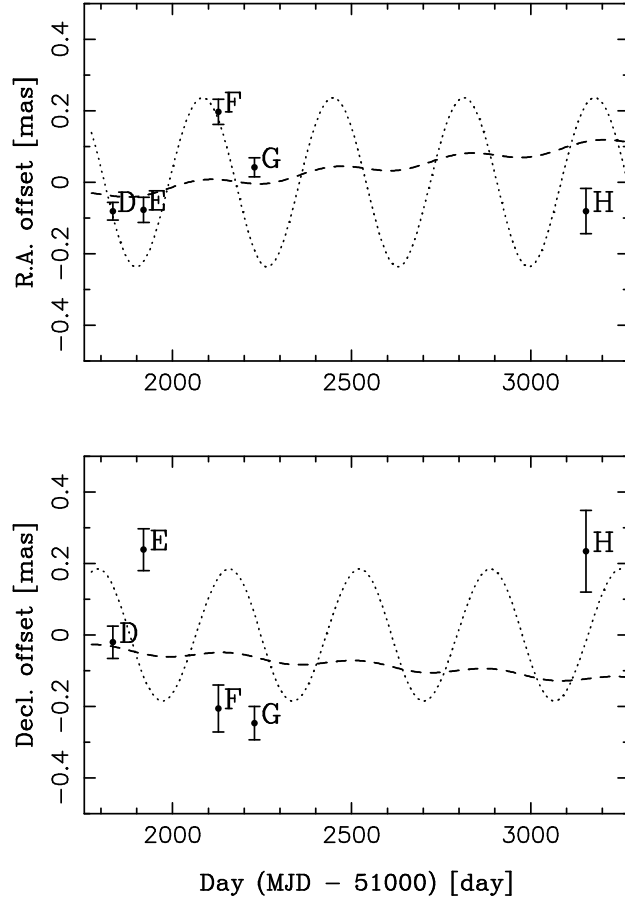


Fig. 2.— Peak position of the KR143 phase-referenced images with respect to ICRF 0244+624 at 15 GHz. The top and the bottom plots show the time variation in right ascension and declination, respectively. The zero position in each plot represents the unweighted average for the five epochs. The error bars represent the position measurement error. The dashed lines represent the least-square analysis result for the proper motion and annual parallax. The dotted lines represent an annual parallax for a source at 4-kpc away from the Sun.

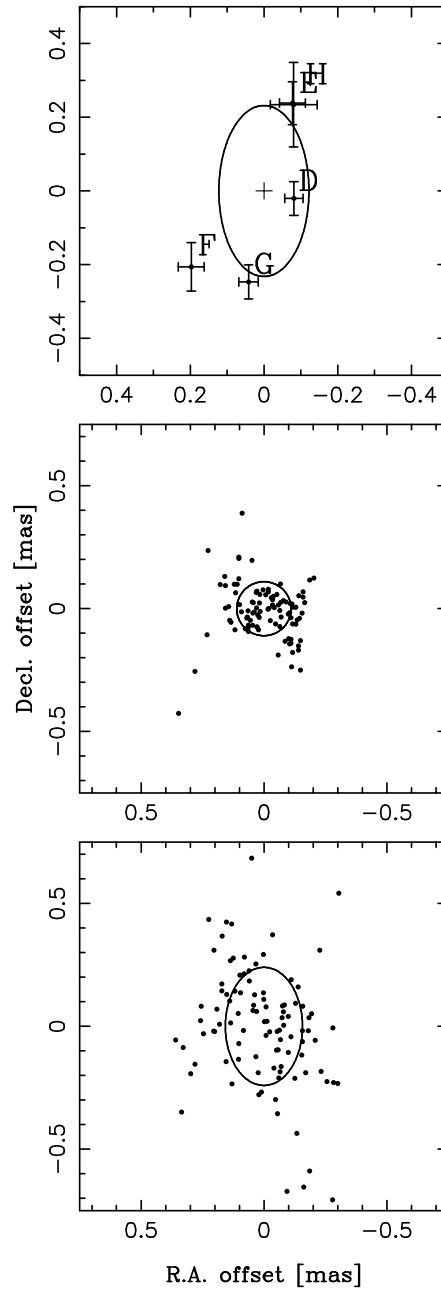


Fig. 3.— KR143’s image peak position relative to ICRF 0244+624 at 15 GHz. The top plot shows the observation results with the error bars, and the middle and bottom plots show results of 100 trials of the observation simulation for KR143 and ICRF 0244+624 with the static tropospheric excess path length error of 3 and 6 cm to the zenith, respectively. The central cross mark at the origin in the top plot is located at the unweighted average position of the measurements. The ellipses represent $1\text{-}\sigma$ for the distributions.

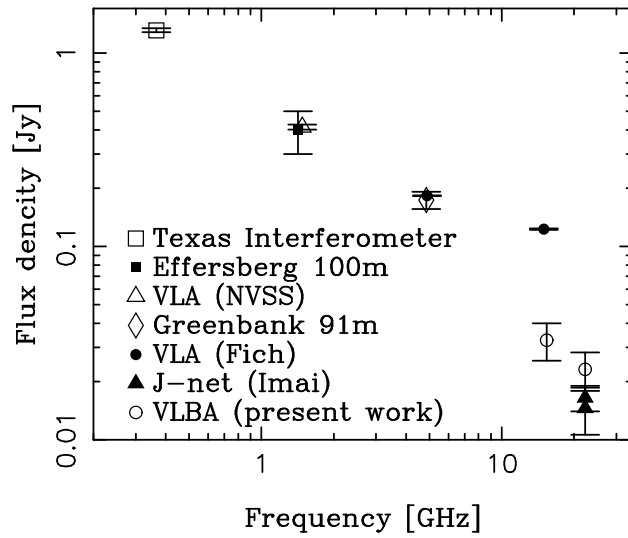


Fig. 4.— Radio spectrum of KR143. The abscissa is an observing frequency, and the ordinate is a flux density (both in logarithmic scales). The open square, the filled square, the open triangle, the open diamond, the filled triangle, and the filled circle represent the Texas survey (Douglas et al. 1996), 21-cm radio continuum survey (Kallas & Reich 1980), NRAO VLA Sky Survey (NVSS) (Condon et al. 1998), the 6-cm northern sky catalogue (Becker et al. 1991), the outer galaxy VLA survey (Fich 1986), and the J-net VLBI observations (Imai 2001), respectively. The open circles represent the current VLBA observation results which are averaged at each frequency.

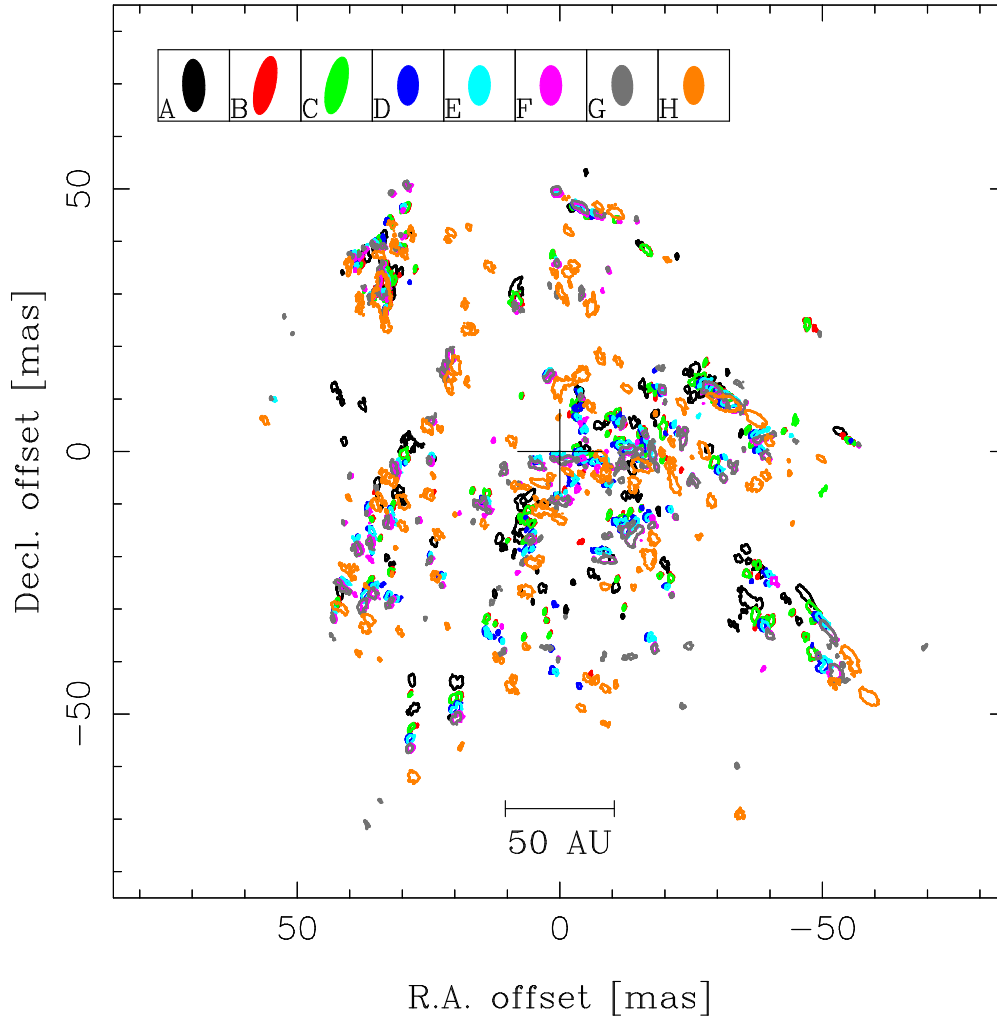


Fig. 5.— Spatial distribution of S Per H_2O masers in the eight epochs. The central cross represents the error bars of the distribution centroid estimated from the expanding shell flow model fitting described in Section 4.2. The outlines of maser features represent a $6\text{-}\sigma$ noise-level contour (90, 138, 156, 150, 168, 150, 162, and 138 mJy at epoch A, B, C, D, E, F, G, and H, respectively). The synthesized beams are shown in the upper 1×1 -square mas boxes.

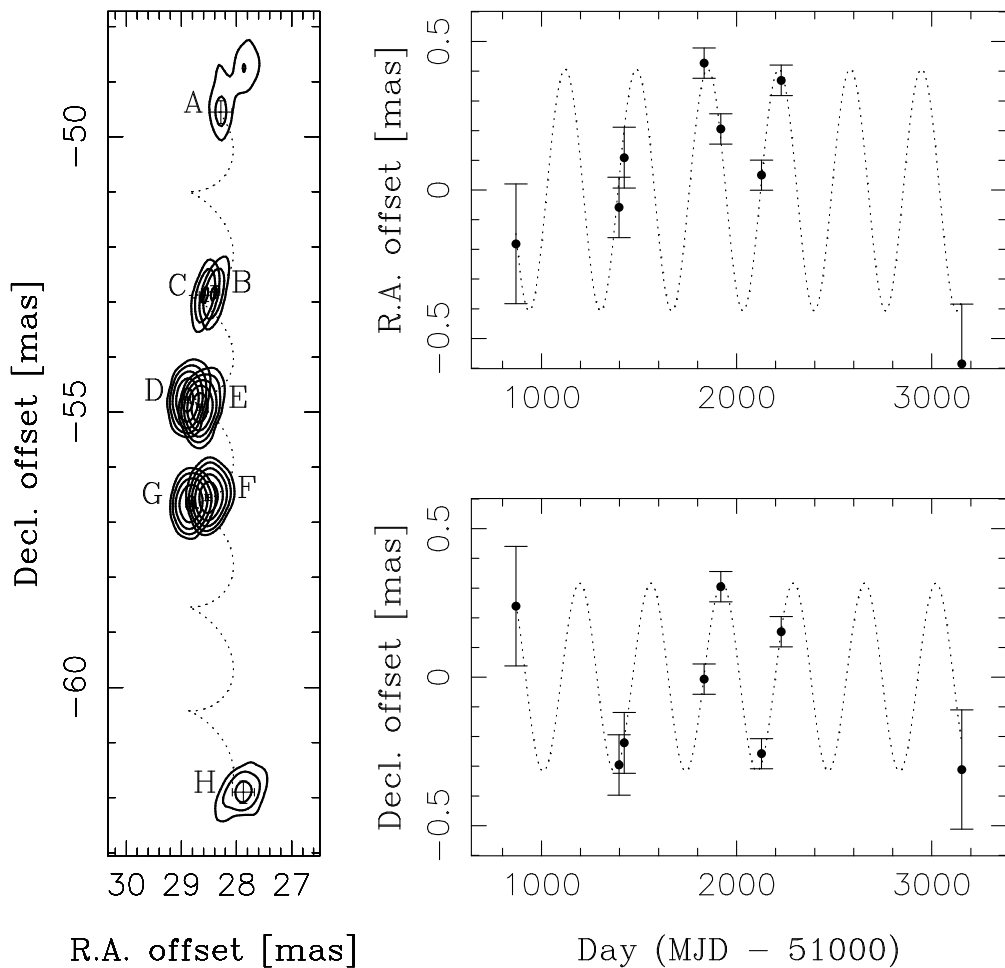


Fig. 6.— Left panel: maser spot motion of S Per on the sky relative to KR143 (spot-ID 39 in Table 4). A dotted line represents the best fit annual parallax and proper motion. The outermost contour shows a $6\text{-}\sigma$ noise level for this channel (96, 144, 162, 156, 180, 162, 174, and 168 mJy at epoch A, B, C, D, E, F, G, and H, respectively), increased by a factor of power of 2. Error bars are root-square-sum of the position measurement error of the brightness peak of the spot, the astrometric error for the pair of the sources, and the diagnostically position error because of the internal structure instability of the maser feature. The right two plots show a residual motion after removing the proper motion. The dotted lines show the best fit annual parallax.

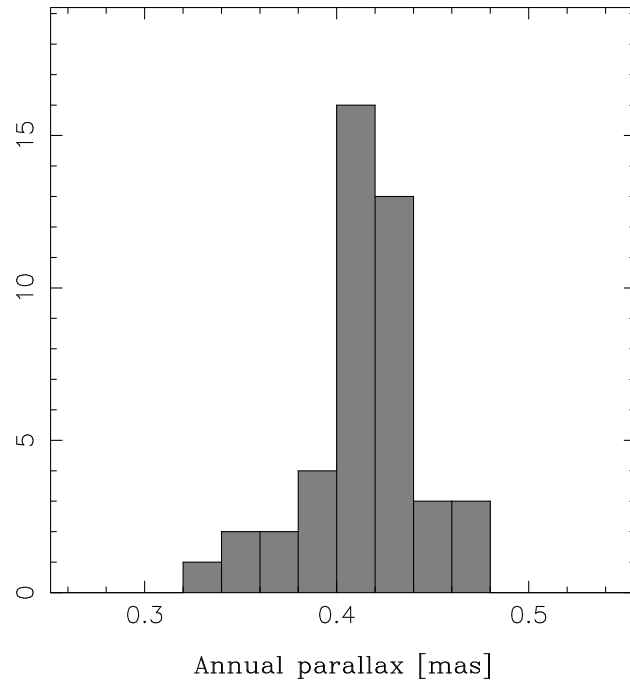


Fig. 7.— Histogram of the annual parallaxes for the 44 maser spots listed in Table 4.

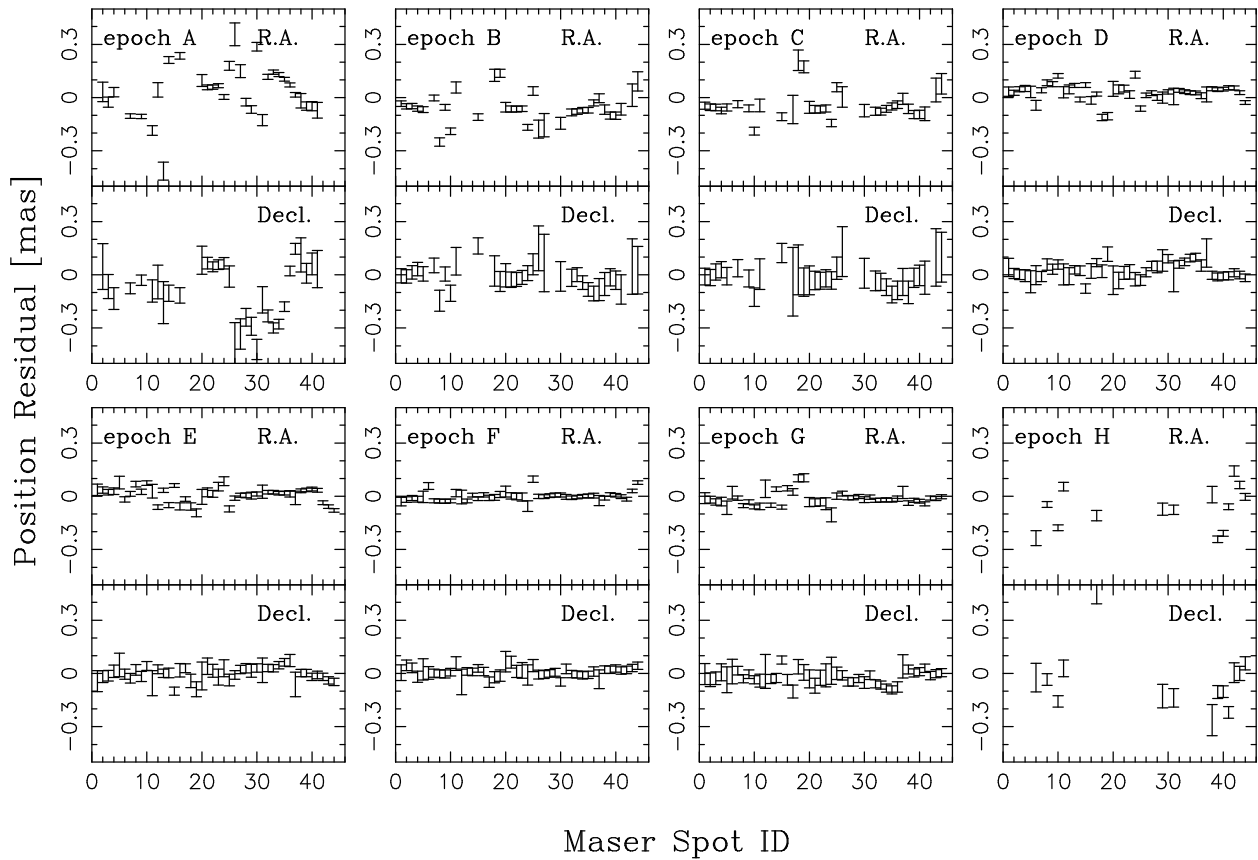


Fig. 8.— Residuals in position of the 44 maser spots after removing the obtained annual parallax of 0.413 mas, proper motions, and initial positions. The abscissa represents the maser spot ID as listed in Table 4, and the ordinate is the position residuals in mas. For each epoch, the position residuals in right ascension and declination are shown in the upper and lower part, respectively. Error bars represent the position measurement error.

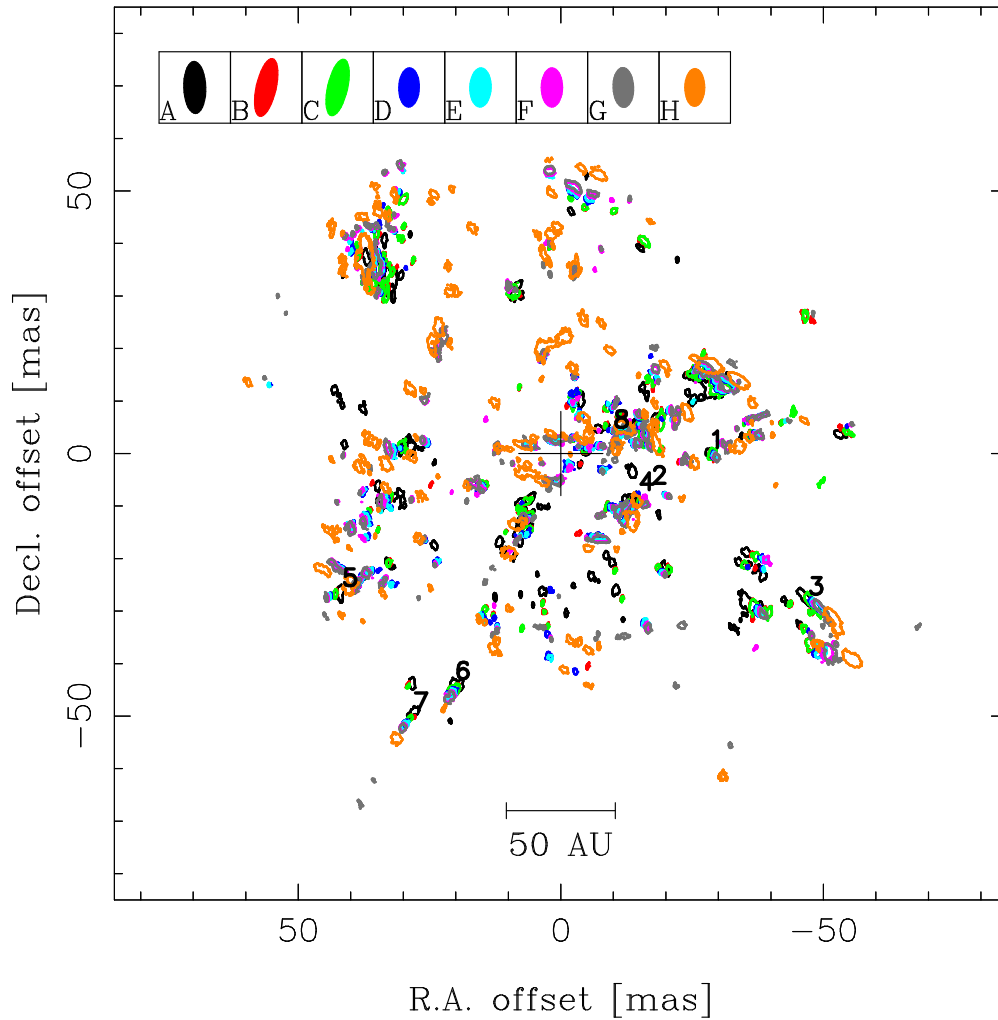


Fig. 9.— Same as Figure 5, but the annual parallax and stellar proper motion are removed. The numbers in the figure (1 to 8) indicate the maser feature-ID which was used for obtaining the stellar annual parallax.

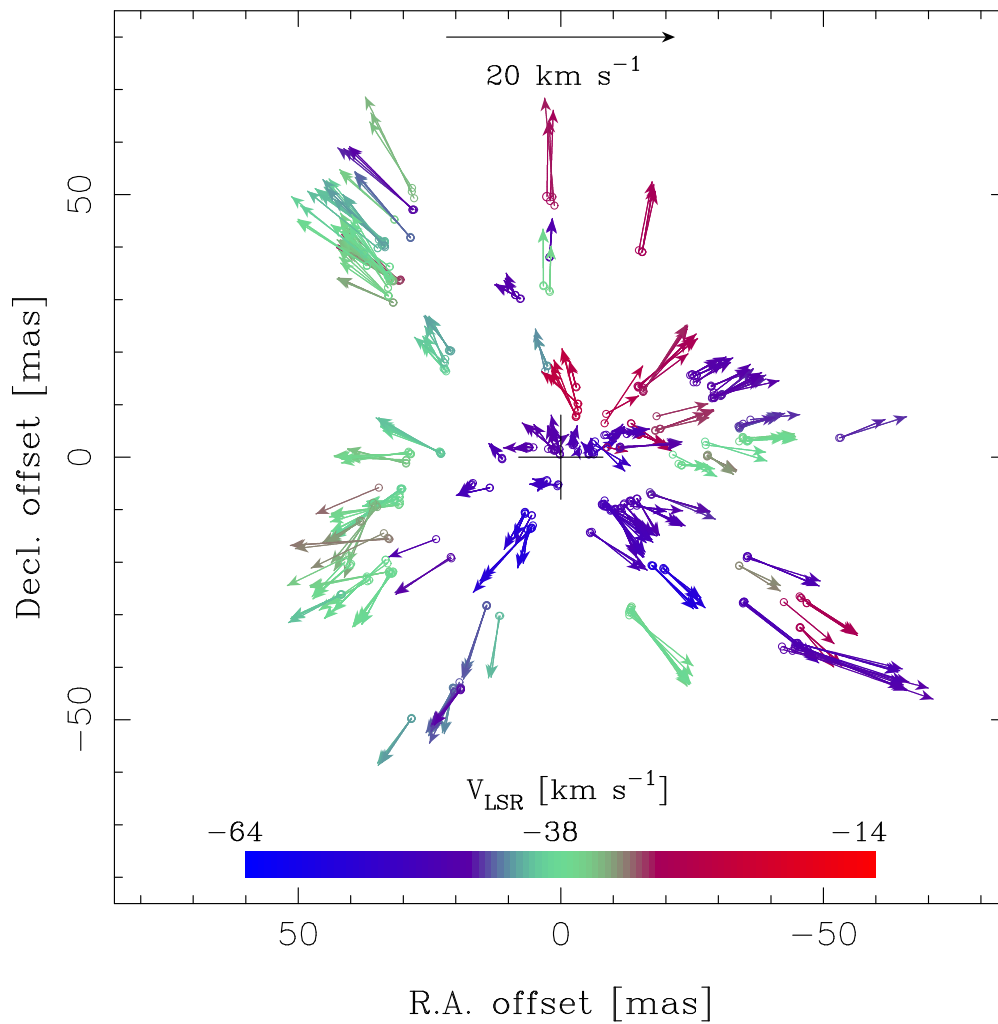


Fig. 10.— Internal proper motions of maser spots of S Per. The color represents the radial velocity.

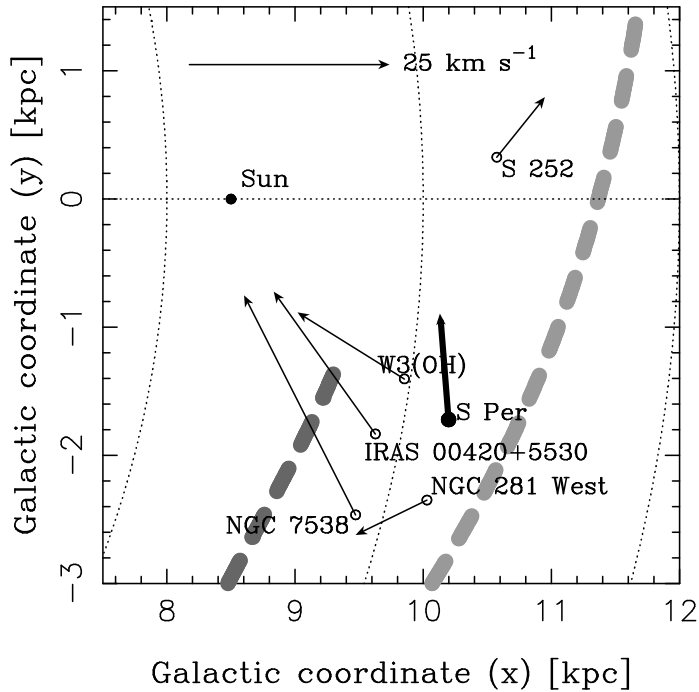


Fig. 11.— Spatial positions and non-circular velocity components of S Per and other maser sources in the Perseus arm projected on the Galactic plane. The depicted sources are W3 (OH) (Xu et al. 2006), NGC 281 West (Sato et al. 2008), IRAS 00420+5530 (Moellenbrock et al. 2009), S 252 (Reid et al. 2009a), NGC 7538 (Moscadelli et al. 2009), and S Per (present paper). A dark-gray dashed curve indicates the Perseus arm obtained from H_{II} survey (Georgelin & Georgelin 1976) while a light-gray dashed curve indicates the one obtained from CO survey (Nakanishi & Sofue 2006). Those traces are adjusted to those for $R_0 = 8.5$ kpc. Dotted curves indicate equi-distances from the Galactic center (8, 10, and 12 kpc).

Table 1: Observation epochs and duty-cycle times for VLBI phase-referencing.

Epoch	Date	Time range (UTC)	t_s at 22 GHz (KR143 – S Per)	t_s at 15 GHz (KR143 – ICRF 0244+624)
A	2000 Nov 21	03:10 – 08:10	40 s	–
B	2002 May 3	16:26 – 21:26	40 s	–
C	2002 May 29	14:44 – 19:44	40 s	–
D	2003 Jul 13	10:48 – 17:48	35 s	60 s
E	2003 Oct 7	05:10 – 12:09	35 s	60 s
F	2004 May 2	15:29 – 22:27	35 s	60 s
G	2004 Aug 11	08:46 – 15:46	35 s	60 s
H	2007 Feb 22	20:03 – 03:01	35 s	60 s

Table 2: Observed pairs of sources in our monitoring program.

Target	Phase-referencing calibrator	Separation angle	Frequency	Epoch
KR143 ^a	S Per	0.2°	22.2 GHz	A – H
KR143	ICRF 0244+624 ^b	4.8°	15.3 GHz	D – H

^aKR143 is a positional reference of S Per in VLBI phase-referencing at 22 GHz.

^bICRF 0244+624 is a positional reference of KR143 in VLBI phase-referencing at 15 GHz.

Table 3: Determined KR143's positions.

Source	RA (J2000)	Dec (J2000)
KR143 ^a	$2^{\text{h}}22^{\text{m}}33^{\text{s}}.520836 \pm 0^{\text{s}}.000018$	$+58^{\circ}48'13''.944455 \pm 0''.000256$

^aThe positional reference in the International Celestial Reference Frame (ICRF) is ICRF 0244+624. The position error of ICRF 0244+624 in ICRF (0.124 and 0.228 mas in right ascension and declination, respectively) is taken into consideration. This position is located at the origin of Figure 2 and of the top plot in Figure 3.

TABLE 4
 PROPER MOTIONS AND PARALLAXES FOR THE S PER H₂O MASER SPOTS.

Spot ID (Feature ID)	$\Delta\alpha_A$ [mas]	$\Delta\delta_A$ [mas]	V_{LSR} [km s ⁻¹]	π [mas]	$\mu_\alpha \cos \delta$ [mas yr ⁻¹]	μ_δ [mas yr ⁻¹]
1(1)	-27.85 ± 0.11	0.11 ± 0.03	-33.58	0.417 ± 0.047	-0.95 ± 0.04	-1.40 ± 0.01
2(1)	-27.86 ± 0.10	0.26 ± 0.03	-33.79	0.398 ± 0.041	-0.93 ± 0.03	-1.43 ± 0.01
3(1)	-27.86 ± 0.10	0.28 ± 0.03	-34.00	0.398 ± 0.040	-0.93 ± 0.03	-1.44 ± 0.01
4(1)	-27.89 ± 0.10	0.27 ± 0.03	-34.21	0.425 ± 0.042	-0.92 ± 0.03	-1.42 ± 0.01
5(1)	-27.98 ± 0.12	0.48 ± 0.04	-34.42	0.410 ± 0.051	-0.89 ± 0.04	-1.50 ± 0.01
6(2)	-17.31 ± 0.17	-7.16 ± 0.03	-45.59	0.403 ± 0.046	-1.35 ± 0.05	-1.43 ± 0.01
7(3)	-46.82 ± 0.10	-27.82 ± 0.03	-29.57	0.412 ± 0.039	-1.23 ± 0.03	-1.66 ± 0.01
8(3)	-45.69 ± 0.12	-26.81 ± 0.03	-29.57	0.454 ± 0.039	-1.37 ± 0.04	-1.73 ± 0.01
9(3)	-46.83 ± 0.10	-27.79 ± 0.03	-29.78	0.429 ± 0.040	-1.21 ± 0.03	-1.66 ± 0.01
10(3)	-45.84 ± 0.10	-26.86 ± 0.03	-29.78	0.470 ± 0.038	-1.32 ± 0.03	-1.71 ± 0.01
11(3)	-45.46 ± 0.09	-26.52 ± 0.03	-30.21	0.352 ± 0.043	-1.37 ± 0.03	-1.79 ± 0.01
12(4)	-14.57 ± 0.15	-7.89 ± 0.04	-47.06	0.475 ± 0.052	-0.81 ± 0.05	-1.76 ± 0.01
13(4)	-13.52 ± 0.14	-8.53 ± 0.03	-47.69	0.431 ± 0.041	-1.21 ± 0.04	-1.50 ± 0.01
14(4)	-13.24 ± 0.14	-8.37 ± 0.03	-48.12	0.411 ± 0.042	-1.30 ± 0.04	-1.54 ± 0.01
15(4)	-12.08 ± 0.11	-8.78 ± 0.03	-48.12	0.372 ± 0.039	-0.88 ± 0.04	-1.72 ± 0.01
16(4)	-13.28 ± 0.14	-8.37 ± 0.03	-48.33	0.412 ± 0.043	-1.29 ± 0.04	-1.54 ± 0.01
17(4)	-11.36 ± 0.13	-10.00 ± 0.03	-48.33	0.449 ± 0.042	-0.90 ± 0.04	-1.54 ± 0.01
18(4)	-7.85 ± 0.12	-9.12 ± 0.03	-49.38	0.404 ± 0.043	-1.26 ± 0.04	-1.72 ± 0.01
19(4)	-7.81 ± 0.11	-8.95 ± 0.03	-49.59	0.386 ± 0.043	-1.27 ± 0.04	-1.77 ± 0.01
20(5)	41.93 ± 0.10	-26.14 ± 0.04	-39.90	0.384 ± 0.051	0.28 ± 0.03	-1.57 ± 0.01
21(5)	41.93 ± 0.10	-26.15 ± 0.03	-40.11	0.403 ± 0.043	0.27 ± 0.03	-1.56 ± 0.01
22(5)	41.88 ± 0.10	-26.15 ± 0.03	-40.32	0.425 ± 0.042	0.27 ± 0.03	-1.54 ± 0.01
23(5)	41.83 ± 0.10	-26.15 ± 0.03	-40.53	0.401 ± 0.045	0.28 ± 0.03	-1.56 ± 0.01
24(6)	20.53 ± 0.10	-43.94 ± 0.03	-43.48	0.472 ± 0.047	-0.15 ± 0.03	-1.91 ± 0.01
25(6)	20.29 ± 0.10	-44.08 ± 0.03	-43.69	0.332 ± 0.042	-0.08 ± 0.03	-1.91 ± 0.01
26(6)	20.04 ± 0.10	-44.47 ± 0.03	-43.90	0.405 ± 0.041	-0.03 ± 0.03	-1.82 ± 0.01
27(6)	20.12 ± 0.12	-44.67 ± 0.03	-44.11	0.425 ± 0.041	-0.07 ± 0.04	-1.77 ± 0.01
28(6)	20.28 ± 0.14	-44.78 ± 0.03	-44.32	0.419 ± 0.042	-0.13 ± 0.04	-1.75 ± 0.01
29(6)	20.27 ± 0.12	-44.75 ± 0.03	-44.53	0.426 ± 0.041	-0.13 ± 0.04	-1.78 ± 0.01
30(6)	19.21 ± 0.10	-44.09 ± 0.03	-44.74	0.425 ± 0.040	-0.05 ± 0.03	-1.72 ± 0.01
31(6)	20.26 ± 0.13	-44.81 ± 0.03	-44.74	0.418 ± 0.044	-0.14 ± 0.04	-1.78 ± 0.01
32(6)	19.10 ± 0.10	-43.90 ± 0.03	-44.96	0.417 ± 0.039	-0.04 ± 0.03	-1.78 ± 0.01
33(6)	19.05 ± 0.10	-43.97 ± 0.03	-45.17	0.408 ± 0.039	-0.03 ± 0.03	-1.75 ± 0.01
34(6)	19.03 ± 0.10	-44.06 ± 0.03	-45.38	0.419 ± 0.039	-0.03 ± 0.03	-1.73 ± 0.01
35(6)	19.03 ± 0.10	-44.14 ± 0.03	-45.59	0.430 ± 0.039	-0.04 ± 0.03	-1.72 ± 0.01
36(6)	19.06 ± 0.10	-44.22 ± 0.03	-45.80	0.433 ± 0.041	-0.06 ± 0.03	-1.73 ± 0.01
37(6)	19.11 ± 0.10	-44.32 ± 0.04	-46.01	0.454 ± 0.050	-0.09 ± 0.03	-1.74 ± 0.01
38(7)	28.43 ± 0.09	-49.64 ± 0.03	-41.79	0.430 ± 0.037	0.02 ± 0.03	-1.93 ± 0.01
39(7)	28.47 ± 0.09	-49.79 ± 0.03	-42.01	0.430 ± 0.037	-0.00 ± 0.03	-1.89 ± 0.01

TABLE 4—*Continued*

Spot ID (Feature ID)	$\Delta\alpha_A$ [mas]	$\Delta\delta_A$ [mas]	V_{LSR} [km s ⁻¹]	π [mas]	$\mu_\alpha \cos \delta$ [mas yr ⁻¹]	μ_δ [mas yr ⁻¹]
40(7)	28.46 ± 0.09	-49.80 ± 0.03	-42.22	0.422 ± 0.037	-0.01 ± 0.03	-1.89 ± 0.01
41(7)	28.48 ± 0.09	-49.83 ± 0.03	-42.43	0.428 ± 0.037	-0.04 ± 0.03	-1.87 ± 0.01
42(8)	-9.84 ± 0.15	3.81 ± 0.03	-47.91	0.404 ± 0.041	-0.67 ± 0.05	-1.03 ± 0.01
43(8)	-9.79 ± 0.11	3.91 ± 0.03	-48.12	0.378 ± 0.039	-0.68 ± 0.03	-1.06 ± 0.01
44(8)	-9.80 ± 0.11	3.98 ± 0.03	-48.33	0.351 ± 0.039	-0.67 ± 0.03	-1.07 ± 0.01

Table 5: Astrometry analysis results of S Per.

Annual parallax	$\pi^* = 0.413 \pm 0.017$ mas (2.42 $^{+0.11}_{-0.09}$ kpc)	
Position (J2000) ^a	Right Ascension:	Declination:
(2000 Nov 21)	2 ^h 22 ^m 51 ^s .7106 \pm 0 ^s .0010	+58°35'11".444 \pm 0".008
Stellar proper motion	$\mu_\alpha^* \cos \delta = -0.49 \pm 0.23$ mas yr ⁻¹	$\mu_\delta^* = -1.19 \pm 0.20$ mas yr ⁻¹

^aThe position errors of ICRF 0244+624 and KR143 are taken into consideration as well as the model fitting error described in Section 4.2. This position is located at the origin of S Per image of Figure 5.